

LiMgPO₄-Coating-Induced Phosphate Shell and Bulk Mg-Doping Enables Stable Ultra-High-Voltage Cycling of LiCoO₂ Cathode

Jiajie Zhong, Wenguang Zhao, Minghao Zhang, Zu-Wei Yin, Zengqing Zhuo,* Shaojian Zhang, Mingjian Zhang, Feng Pan, Bingkai Zhang,* and Zhan Lin*

Stable cycling of LiCoO₂ (LCO) cathode at high voltage is extremely challenging due to the notable structural instability in deeply delithiated states. Here, using the sol-gel coating method, LCO materials (LMP-LCO) are obtained with bulk Mg-doping and surface LiMgPO4/Li3PO4 (LMP/LPO) coating. The experimental results suggest that the simultaneous modification in the bulk and at the surface is demonstrated to be highly effective in improving the high-voltage performance of LCO. LMP-LCO cathodes deliver 149.8 mAh g^{-1} @4.60 V and 146.1 mAh g^{-1} @4.65 V after 200 cycles at 1 C. For higher cut-off voltages, 4.70 and 4.80 V, LMP-LCO cathodes still achieve 144.9 mAh g^{-1} after 150 cycles and 136.8 mAh g^{-1} after 100 cycles at 1 C, respectively. Bulk Mg-dopants enhance the ionicity of Co-O bond by tailoring the band centers of Co 3d and O 2p, promoting stable redox on O^{2-} , and thus enhancing stable cycling at high cut-off voltages. Meanwhile, LMP/LPO surface coating suppresses detrimental surface side reactions while allowing facile Li-ion diffusion. The mechanism of high-voltage cycling stability is investigated by combining experimental characterizations and theoretical calculations. This study proposes a strategy of surface-to-bulk simultaneous modification to achieve superior structural stability at high voltages.

J. Zhong, M. Zhang, S. Zhang, B. Zhang, Z. Lin Guangdong Provincial Key Laboratory of Plant Resources Biorefinery School of Chemical Engineering and Light Industry Guangdong University of Technology Guangzhou 510027, China E-mail: zhangbk@gdut.edu.cn; zhanlin@gdut.edu.cn W. Zhao, Z.-W. Yin, F. Pan School of Advanced Materials Peking University Shenzhen Graduate School, Shenzhen 518055, China Advanced Light Source Lawrence Berkeley National Laboratory Berkeley, CA 94720, USA E-mail: zzhuo@lbl.gov M. Zhang School of Science and Engineering The Chinese University of Hong Kong Shenzhen 518172, China

(D)

The ORCID identification number(s) for the author(s) of this article can be found under https://doi.org/10.1002/smll.202300802

DOI: 10.1002/smll.202300802

1. Introduction

The battery community is deriving an urgent demand for high-energy-density lithium-ion batteries (LIBs), hence the need for cathodes with high-capacity and highvoltage operation.[1,2] LiCoO2 (LCO) has been widely used in electronic devices because of its high theoretical capacity, high volumetric energy density, and good cycling stability.[3,4] The energy density can be improved by operating LCO at high voltages. For example, the usable capacity increases from 140 to 173 mAh g-1 by increasing the upper cut-off voltage of LCO cathode from 4.20 to 4.45 V (vs Li⁺/Li).^[5,6] Unfortunately, pushing the LCO cathode to a higher cut-off voltage tends to induce instabilities in the bulk and at the surface and thus significantly degrades cycle life.[7,8] First, the phase transition from O1 to H1-H3 results in irreversible structural damage, leading to cracks on the surface and gradual diffusion to the interior, followed by electrolyte penetration into the interior of the LCO particles along the

cracks, generating severe interfacial side reactions and the dissolution of high-valent Co ions.^[9,10] Second, at high voltage, with the large proportion of Li (capacity) migrating out of the lattice, the density of states of O²⁻ overlaps with that of Co³⁺/Co⁴⁺, resulting in the oxygen redox in the bulk and oxygen precipitation at the surface, aggravating structural degradations.^[11] Thus, the high-voltage operation of LCO remains a formidable challenge.

To push the cutoff voltage higher and fully utilize the theoretical capacity of LCO, various optimization strategies have been explored and developed, such as elemental doping, surface coating, and suitable electrolyte additives adding. [12–19] Elemental doping has been implemented to suppress phase transition at high voltages (from O3, Monoclinic, O3, H1, H2, H3, to O1 phases with Li ions extraction). However, if LCO cathode is exposed to the direct attack of HF, the operation of a high-voltage charge (>4.5 V) results in many detrimental cathode/electrolyte interface reactions, such as Co dissolution and O loss, which leads to capacity loss. [20,21] On the other hand, surface coating focuses more on LCO surface structure, such as promoting surface charge transfer, mitigating interfacial reactions, and limiting electrolyte

16136829, 2023, 39, Downloaded from https:

/onlinelibrary.wiley.com/doi/10.1002/smll.202300802 by University Town Of Shenzhen, Wiley Online Library on [23/11/2025]. See the Terms

litions) on Wiley Online Library for rules of use; OA articles are governed by the applicable Creative Commons

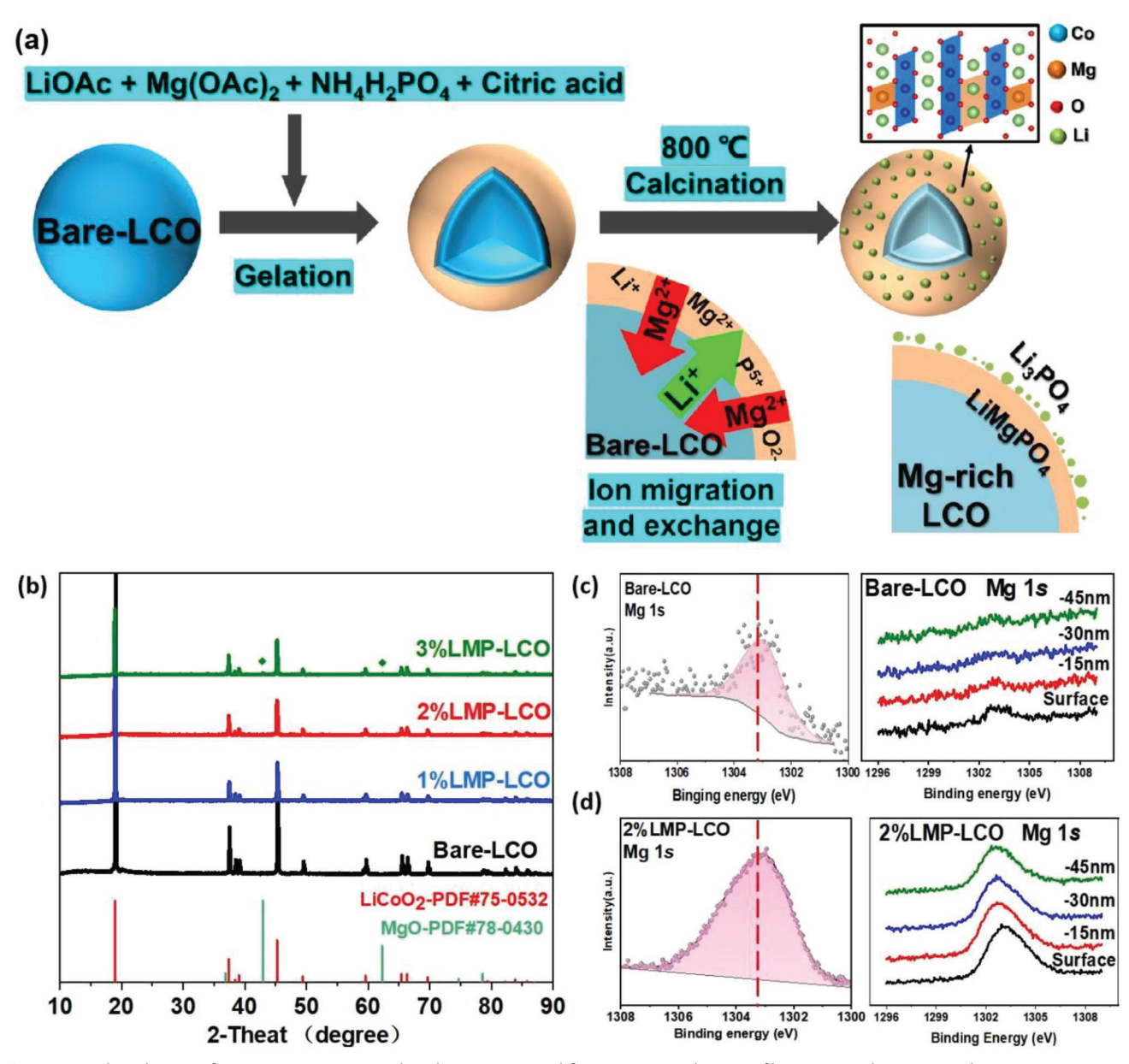


Figure 1. a) The schemes of LMP coating process induced synergistic modification on LCO. b) XRD of bare-LCO and 1%, 2%, and 3%LMP-LCO. c) XPS spectra of Mg 1s in bare-LCO (upper inset) and 2%LMP-LCO (lower inset). d) XPS etching profiles of Mg in bare-LCO (upper inset) and 2%LMP-LCO (lower inset).

penetration. But simple coating without causing internal structural change to LCO is hard to suppress the phase transition of LCO. Therefore, co-optimizing the bulk and surface properties is the key toward better high-voltage operation of LCO than doping or coating alone.

In this work, we demonstrate that a cost-effective LiMgPO₄ (LMP) coating on commercial LCO cathodes (bare-LCO) enables stable ultrahigh voltage cycling (>4.60 V). The schematic of the LMP coating process and chemical composition of bulk Mgdoped and surface phosphate-coated LCO samples (LMP-LCO) are displayed in **Figure 1a**. During coating processes that involve post-thermal treatment, partial Mg-ions in the coating layer diffuse into the bulk structure of LCO, leading to Mg-doping at

Li-sites. Meanwhile, the substituted Li-ions in LCO also diffuse to the outer surface of LCO along with the coating sources (Li⁺ and PO_4^{3-}) to form Li₃PO₄. Thus, LMP-LCO provides a LMP/LPO (LiMgPO₄/Li₃PO₄) protection layer on the surface of LCO and stabilizes the structure of the LCO host via Mg-doping as well as the interface between LCO and the electrolyte. After the bulk and surface modification, LMP-LCO achieves a discharge capacity of 149.8 mAh g⁻¹@4.60 V and 146.1 mAh g⁻¹ @4.65 V after 200 cycles at a current rate of 1 C. The electrochemical cycling of LMP-LCO at cutoff voltages of 4.70 and 4.80 V still get very good cycle stability comparable to that at 4.60 and 4.65 V. As confirmed by both experimental characterization and theoretical calculations, the improved high-voltage electrochemical

www.advancedsciencenews.com

____3111Q11

16136829, 2023, 3, 9. Downloaded from https://onlinelbrary.wi.ele.com/doi/10.1002/smll.202308020 by University Town Of Shenzhen, Wiley Online Library on [23/112025]. See the Terms and Conditions (https://onlinelibrary.wiley.com/terms-and-conditions) on Wiley Online Library for rules of use; OA articles are governed by the applicable Creative Commons Licensee

www.small-journal.com

performance is ascribed to the full utilization of structural stability through the creation of an Mg-doped bulk structure.

2. Results and Discussion

2.1. Phase Composition and Structure of Bare-LCO and LMP-LCO

The LMP-LCO cathodes are prepared by a sol-gel method (see the Experimental section). the X-ray diffraction (XRD) patterns show that the original (003) peak (emerging at $\approx 19.6^{\circ}$), a direct response to the lattice parameter *c*, shifts to lower angles with the weight of LMP coating increasing, which reflects an increase of lattice parameter c. Thus, after the sol–gel process is completed, LMP coating leads to a slight increase in the crystal constants of LCO with no change in the crystal structure (Figure 1b). The density functional theory (DFT) method is used to obtain the lattice parameters (Table S1, Supporting Information), which suggests a increased parameter lattices of c and V in LMP-LCO. Interestingly, with the increase of weight percentages of LMP, there is no diffraction signal belonging to the LMP, but the diffraction signal of crystalline MgO appears in 3%LMP-LCO, indicating that the introduction of a large amount (3 wt.%) of precursor magnesium salt leads to MgO formation and the amount of crystalline phosphate is too small to identify them. X-ray photoelectron spectroscopy (XPS) with depth-profiling data has been used to explore the composition changes of bare-LCO and LMP-LCO (Figure 1c,d). Unexpectedly, for bare-LCO, Mg 1s spectrum displays a small peak area with binding energy (BE) of 1303.4 eV,[22] indicating bare-LCO itself contains a certain amount of Mg²⁺. For LMP-LCO, unsurprisingly, the peak intensity of Mg²⁺ spectrum is greatly increased, and the signal of P⁵⁺ spectrum takes place at BE of 133.0 eV, which is attributed to P–O in phosphate (Figure S1a,b, Supporting Information). XPS depth profile analysis supports that element P distribution within several tens of nanometers in LMP-LCO due to the high-temperature calcination process (Figure S1c,d, Supporting Information). In addition, the Co 2p spectrum of bare-LCO and LMP-LCO displays similar satellite features (Figure S2a,c, Supporting Information), indicating the chemical environment of Co remains unchanged after LMP coating. In O 1s spectra (Figure S2b,d, Supporting Information), the peak located at 529.6 eV is characteristic of oxygen ions in the LCO crystal lattice. The peak emerging at 531.6 eV is associated with oxygen-containing absorbed species (such as C=O in CO₃²⁻) on the LCO surface with a deficient coordination.^[23-25] The O 1s spectra peak of ≈532.62 eV is attributed to P-O in phosphate. Indeed, the use of ion sputtering for depth profiling may induce particle mixing and the creation of different phases. Therefore, XPS depth profiling alone hardly provides quantitative information evaluating the doping level of Mg-dopants and detecting possible places of Mg-dopants.

High-resolution transmission electron microscopy (HR-TEM) is used to further illustrate the changes between the pristine bare-LCO and LMP-LCO (Figure 2a,b). A clear lattice stripe with Co and Li layers (a crystal spacing of d=0.455 nm) extending to the very edge of atomic planes is observed in the bare-LCO (Figure 2a). A fast Fourier transform (FFT) in the selected region 1 allows the observation of a very well-oriented (003) crystal plane (Figure 2c,d). [26] Meanwhile, in contrast, a surface coating layer with a thickness of $\approx 5-10$ nm is readily observed after the

LMP coating, where the red dashed line indicates the boundary between the LCO and the surface coating layer. FFT images in regions 2 and 3 (Figure 2e,f) suggest that the crystal structure of the reconstruction layer consists primarily of olivine structure LiMgPO₄ (well-oriented (020), (211), and (220) crystal faces), with a few and dotted distribution of orthorhombic structure Li₃PO₄ ((141), (131), and (211) crystal faces) at the outmost surface of particles. The presence of the Li₃PO₄ indicates that some Mg-ions in the sol-gel may diffuse into the bulk phase of LCO and replace Li-ions in LCO since a smaller ionic radius of Mg-ion (0.72 Å) than Li-ion (0.76), in which the following chemical reaction takes place during calcination: $3Li^+ + 2Mg^{2+} + 2PO_4^{3-} + 2LiCoO_2 \rightarrow$ $(LiMg)Co_2O_4 + LiMgPO_4 + Li_3PO_4$. More similar HR-TEM structure characterizations for bulk layered structure and surface coating layer are identified in Figure S3 (Supporting Information), further confirming the intact bulk structure and a seamless coating layer of LMP-LCO particles. Further cross-section elemental distribution of one LMP-LCO particle visualized by HR-TEM energy dispersive spectrometer (EDS) mapping (Figure 2g-j) shows an overall homogeneous distribution of the elements Co, O, and Mg in the bulk. In particular, element Mg is distributed homogeneously in the bulk and no obvious segregation is observed on the surface, indicating Mg-ions may diffuse into bulk LCO. In addition, scanning electron microscopy (SEM) images show that the particles of the bare-LCO powder are very regularly with a diameter of \approx 3–5 µm (Figure 2k; Figure S4, Supporting Information). After the LMP coating process, the spherical morphology of 2% and 3%LMP-LCO (Figure 2m) is also very smooth with no visible rough spots or pores compared to 1% LMP-LCO samples (Figure 2l,n). The uniformly elemental distributions are also visualized by SEM EDS mapping (Figure S5, Supporting Information). The above observations strongly confirm that LMP/LPO surface coating layer with a thickness of \approx 5-10 nm is smoothly, uniformly, and coherently integrated on crystalline LCO, which direct contact between the active substance and the electrolyte (especially at high voltages) is avoided, thus inhibiting interfacial side reactions.

2.2. Improved Cycling Stability at the Ultra-High Voltage

To reveal the advantages of the LMP coating modification, the cycling stability and rate capability of bare-LCO and LMP-LCO cathodes are cycled in half cells with a high cut-off voltage (Figure 3). The corresponding discharge-charge voltage profiles of cells with bare-LCO and LMP-LCO cathodes are generally consistent with the characteristic profiles of Li/LCO in carbonate-based electrolytes (Figures S6-S9, Supporting Information). As presented in Figure 3a, under the cut-off voltage of 4.60 V, the 2%LMP-LCO archives a reversible capacity of 149.8 mAh g⁻¹ at 1 C after 200 cycles, corresponding to a capacity retention of 73.42% and Coulombic efficiency of ≈99.9%, while the pristine bare-LCO cathode displays only 82.0 mAh g⁻¹ and 42.44% capacity retention after 100 cycles. We note that the bare-LCO exhibits rapid capacity fading and decreasing average discharge voltage compared to the LMP-LCO. At a cut-off voltage of 4.65 and 4.70 V, the capacity retention of 2%LMP-LCO is 71.76% (146.1 mAh g⁻¹) after 200 cycles and 67.02% (144.9 mAh g^{-1}) after 150 cycles at 1 C, respectively (Figure 3b,c). To further evaluate the stability of the

16136829, 2023, 39, Downloaded from https:

Wiley Online Library on [23/11/2025]. See the Terms

conditions) on Wiley Online Library for rules of use; OA articles are governed by the applicable Creative Commons

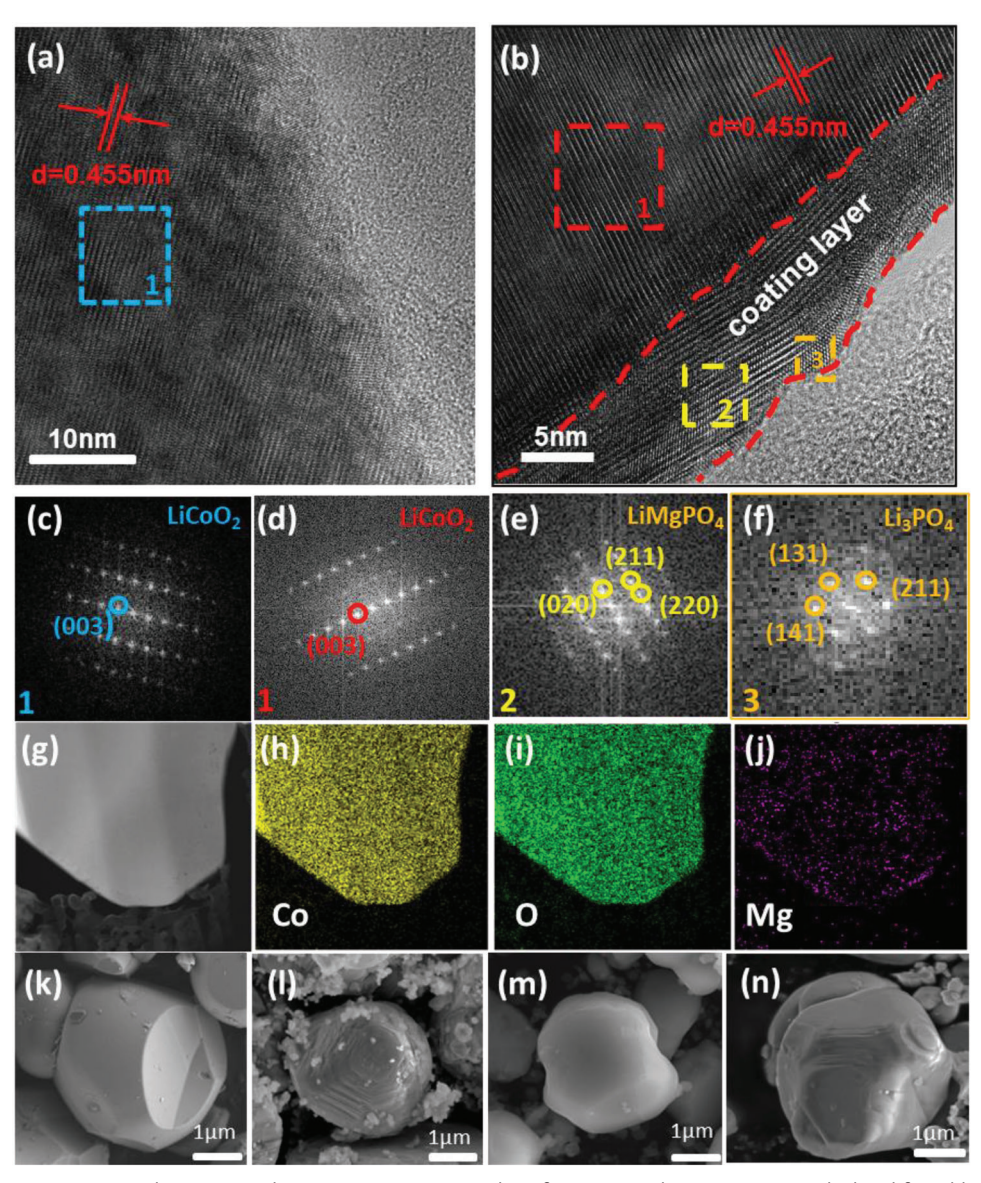


Figure 2. a,b) TEM/HRTEM images bare-LCO and 2%LMP-LCO, respectively. c–f) Corresponding FFT images calculated from blue zone (c), red zone (d), yellow zone (e), and orange zone (f), respectively. g–j) The cross-section TEM EDS elemental mappings of Co, O, and Mg (scale bar: 500 nm) on one 2%LMP-LCO particle. k) SEM images of bare-LCO, l) 1%LMP-LCO, m) 2%LMP-LCO, and n) 3%LMP-LCO, respectively.

LMP-LCO, cells based on LMP-LCO are also tested at the ultrahigh cut-off of voltage (4.80 V). After two activation cycles at 0.2 C, the first cycle (1 C) discharge specific capacity of 2%LMP-LCO is 217.2 mAh g⁻¹ with a coulomb efficiency of 96.78%. After 100 cycles, the capacity retention of 2% LMP-LCO is 62.98% (136.8 mAh g⁻¹). With the increase in cut-off voltage, the cycling performance effects of coating change become more obvious. Moreover, the 1%LMP-LCO and 3%LMP-LCO cathodes exhibit less reversible capacity and higher polarization in the charge/discharge profiles compared to the 2%LMP-LCO, emphasizing the 2%LMP-LCO is the optimal amount in the coating process (Figure 3d).

There are, however, two unexpected observations in the electrochemical cycling of LMP-LCO. Specifically, first, in all cycling performances at different cut-off voltages for both bare-LCO and

LMP-LCO, what is striking, really remarkable, that initial capacity quickly loses within the first five cycles due to interfacial reaction. After the five cycles' charging/discharging processes, the amount of capacity loss is greatly reduced, less than 0.18 mAh g⁻¹ per cycle. In the whole 200 cycles, the first five cycles contribute 52% and 51% of capacity loss of 2%LMP-LCO cathode at a cut-off voltage of 4.60 V and 4.65 V (Figure 3a,b), respectively. A similar observation is also found for 4.7 V and 4.8 V cycling of LMP-LCO. It indicates that capacity fading may be caused by surface cobalt dissolution during the first five cycles.^[27] Second, for the 2%LMP-LCO electrodes, the retention of the discharge capacity for the 4.70 V and 4.80 V cutoff is 78% and 72% for 10–150 cycles and 10–100 cycles, respectively. The cycle stability with 4.70 V and 4.80 V cutoffs is comparable to that for the 4.60 and 4.65 V charging conditions, which is in contrast with the

16136829, 2023, 39, Downlo

elibrary.wiley.com/doi/10.1002/smll.202300802 by University Town Of Shenzhen, Wiley Online Library on [23/11/2025]. See the Terms and Conditions (https://www.com/doi/10.1002/smll.202300802 by University Town Of Shenzhen, Wiley Online Library on [23/11/2025]. See the Terms and Conditions (https://www.com/doi/10.1002/smll.202300802 by University Town Of Shenzhen, Wiley Online Library on [23/11/2025]. See the Terms and Conditions (https://www.com/doi/10.1002/smll.202300802 by University Town Of Shenzhen, Wiley Online Library on [23/11/2025]. See the Terms and Conditions (https://www.com/doi/10.1002/smll.202300802 by University Town Of Shenzhen, Wiley Online Library on [23/11/2025]. See the Terms and Conditions (https://www.com/doi/10.1002/smll.202300802 by University Town Of Shenzhen, Wiley Online Library on [23/11/2025]. See the Terms and Conditions (https://www.com/doi/10.1002/smll.202300802 by University Town Of Shenzhen, Wiley Online Library on [23/11/2025]. See the Terms and Condition (https://www.com/doi/10.1002/smll.202300802 by University Town Of Shenzhen, Wiley Online Library on [23/11/2025]. See the Terms and Condition (https://www.com/doi/10.1002/smll.202300802 by University Town Of Shenzhen, Wiley Online Library on [23/11/2025]. See the Terms and Condition (https://www.com/doi/10.1002/smll.202300802 by University Town Of Shenzhen, Wiley Online Library on [23/11/2025]. See the Terms of the University Town Of Shenzhen (https://www.com/doi/10.1002/smll.202300802 by University Town Of Shenzhen (https://www.com/doi/10.1002). The University Town Of Shenzhen (https://www.com/d

ms) on Wiley Online Library for rules of use; OA articles are governed by the applicable Creative Commons Licenso

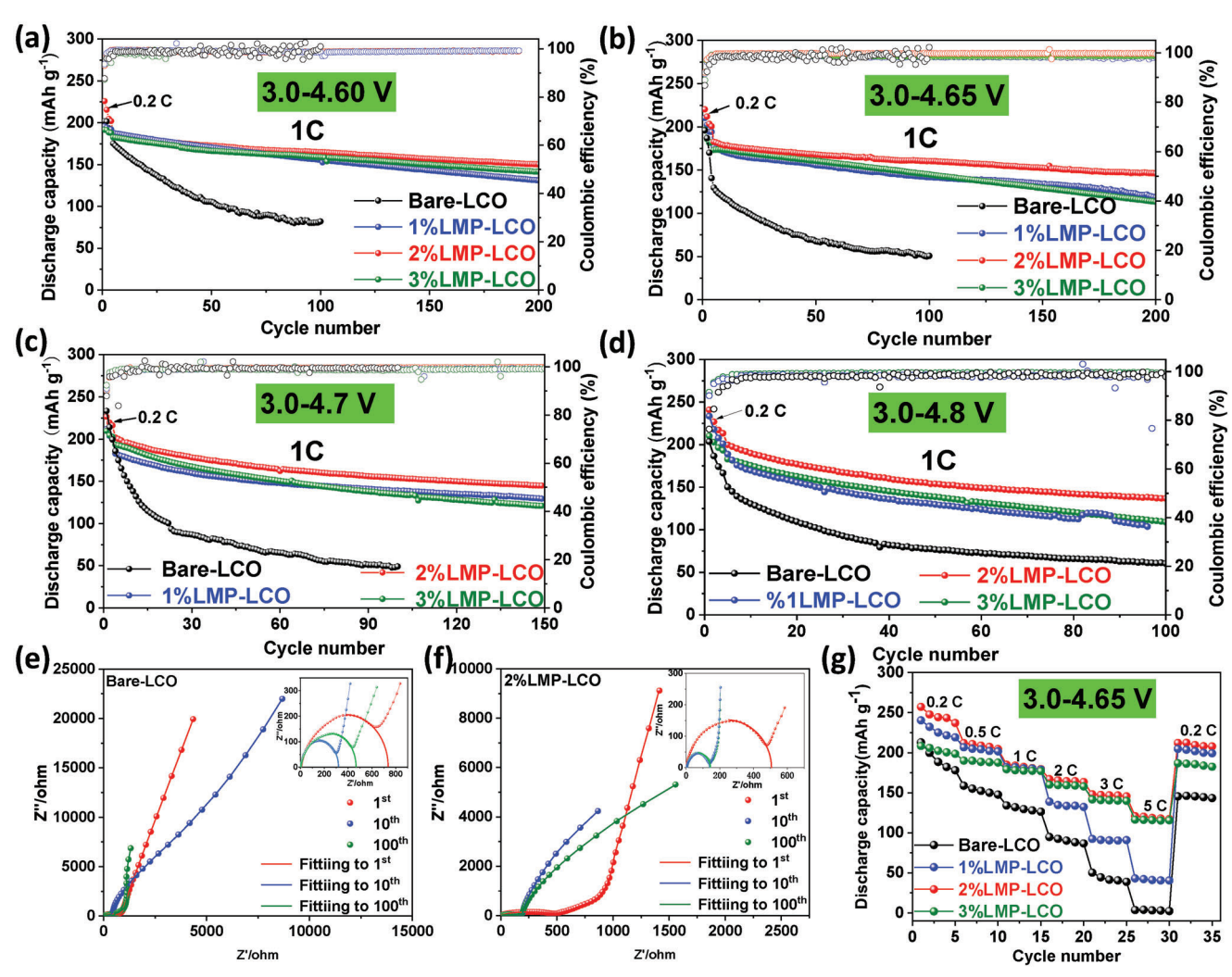


Figure 3. Improved electrochemical performance of LMP-LCO. a-d) Cycling performance of bare-LCO and 1%/2%/3% LMP-LCO within a) 3.0-4.60 V, b) 3.0-4.65 V, c) 3.0-4.70 V, and d) 3.0-4.80 V (vs Li/Li⁺) at 1 C. e,f) Electrochemical impedance spectra of the bare-LCO and 2%LMP-LCO after the 1st, 10th, and 100th cycles, respectively. g) Rate performance of the bare-LCO and 1%/2%/3%LMP-LCO, respectively.

expectedly more severe degradation of the bulk and surface structures of LCO at high voltages. [28,29] At 4.80 V, Li, CoO₂ is almost fully delithiated and exists in the O1 structure. This observation implies that the LMP-LCO bulk and LMP/LPO surface are very stable over ultra-high-voltage cycling.

Additionally, to evaluate the interface ion transfer resulting from LMP modification, the combinatorial evaluation is done using the galvanostatic intermittent titration technique (GITT), electrochemical impedance spectroscopy (EIS), and rate capability tests. The GITT curves of bare-LCO and LMP-LCO as a function of specified capacity (Figure S10a,b, Supporting Information) shows that during the charging processes the voltage platform of LMP-LCO (blue line) always displays a lower charged potential than that of bare-LCO (red line) and during discharging processes the voltage platform of LMP-LCO (blue line) always displays a higher discharged potential than that of bare-LCO (red line). By calculating the GITT curve, the polarization changes of the two positive materials can be obtained (Figure S10c,d, Supporting Information). By calculating the voltage variation of each

intermittent charge/discharge, we can see that the polarization of 2%LMP-LCO is smaller than bare-LCO because of the interface reaction inhibited by the coating layer. In Figure S11 (Supporting Information), we calculated the ionic diffusion coefficient of the two positive materials by the GITT and formula D^{GITT} = $\frac{4}{\pi\tau} \left(\frac{m_{\rm B}V_{\rm M}}{M_{\rm B}S}\right)^2 \left(\frac{\Delta E {\rm s}}{\Delta E {\rm t}}\right)^2$. Due to the LMP/LPO coating layer with 3D Liion diffusion channels, the Li-ion diffusion coefficient (DLi+) for 2%LMP-LCO (≈2.1 × 10^{-9} cm² s⁻¹) raises more than one order of magnitude compared to bare-LCO ($\approx 3.5 \times 10^{-10} \text{ cm}^2 \text{ s}^{-1}$).

The above conclusion is further supported by EIS tests (Figure 3e,f; Table S3 and Figure S12, Supporting Information). The cathode interfacial resistance (R_{CI}) of the bare-LCO cell increases significantly after the first cycle, indicating sluggish Liion transport through the cathode/electrolyte interface. However, the increases in R_{CI} of 2%LMP-LCO cell show only mild variations without a sharp increase, due to a stable cathode/electrolyte interface with a robust charge-transfer kinetic after LMP modification. The rate capability further highlights the advantages of our LMP-LCO samples. By linear fitting of the low-frequency

16136829, 2023, 3, 9, Downloaded from https://onlinelibrary.wiley.com/doi/10.1002/smll.202308020 by University Town Of Shenzhen, Wiley Online Library on [23/11/2025]. See the Terms and Conditions (https://onlinelibrary.wiley.com/terms-and-conditions) on Wiley Online Library for rules of use; OA articles are governed by the applicable Creative Commons Licenses

region of the impedance spectrum (Figure S13, Supporting Information), we obtained the regression equation of the fitting line (Table S4, Supporting Information). The fitting results clearly show that the slope k of the regression equation of bare-LCO is much larger than 2%-LMP-LCO, and a higher slope meant poor ion diffusion. The Li-ion chemical diffusion coefficient (cD^{Li+}) by impedance fitting is also given in Table S5 (Supporting Information) based on the Equations S1 and S2 (Supporting Information). After the 1, 10, and 100 cycles, the cDLi+ in 2%-LMP-LCO is consistently higher than that of bare-LCO. Therefore, it can be concluded that the Li-ion diffusion in coated samples is significantly higher than in bare-LCO. It is important to take note of the difference in the Li diffusion coefficient of EIS compared to that of GITT analysis. The D^{Li+} calculated by GITT is higher than that calculated by EIS. This difference is due to the results obtained under different equilibrium conditions. Compared with the GITT results, the EIS results are obtained under more balanced conditions, and the electrode has a longer relaxation time. At all tested rates, the LMP-LCO exhibits a higher capacity than that of bare-LCO (Figure 3g). 2%LMP-LCO delivers a reversible discharge capacity of 120.8 mAh g⁻¹ after a 25-folds increase in the current rate from 0.2 to 5 C within a cut-off voltage of 4.65 V. When the current rate is reset back to 0.2 C, the capacity of 2%LMP-LCO is almost fully recovered. These results clearly verify that LMP modification guarantees bulk structural stability, high cathode/electrolyte interphase stability, and maintain a benign Li-ion transport. Overall, LMP-LCO shows greatly improved electrochemical performances at ultra-high charging cut-off voltages of 4.60, 4.65, 4.70, and 4.80 V compared with bare-LCO (a comparison of the performances with reports in the literature for high-voltage LCO is also provided in Table S6, Supporting Information).

2.3. Structural Reversibility and Interfacial Stability of LMP-LCO

To illuminate the reasons for the improved electrochemical performances after LMP modification, the cyclic voltammograms (CV) profiles of bare-LCO and LMP-LCO are first studied. Figure 4a,b display the initial five CV profiles carried out between 3.0 and 4.65 V. As can be seen from CV curve, the transformation (two reduction peaks) related to H1-3 \rightarrow O3(II) and O3(II) \rightarrow O3(I) in bare-LCO gradually weakens and tends to disappear with the increase of cycle number. [5,30] In sharp contrast, the two reduction peaks of LMP-LCO could still be observed with the increase in scans. Furthermore, in the CV curves of bare-LCO, the potential differences between the oxidation and reduction peaks at two O3 phase transitions also increase from 0.38 to 0.79 V, and thus the bare-LCO cathode sufferes from larger polarization. Therefore, the LMP-LCO cathode shows excellent reversible redox peaks and very small polarization, which suggests high structural reversibility and contributes to the outstanding electrochemical performances as discussed in Figure 3.

It is noteworthy that for LCO cathode, with the increase of the voltage, oxygen redox ($O^{2-} \leftrightarrow O^{n-}$) in cobalt oxide layers (- CoO_{6-}) begins to contribute to capacity. At high potentials (>4.60 V), due to the overlap of O^{2-} 2p orbit and Co^{3+}/Co^{4+} pair in cobalt oxide layers of LCO, the oxidation/reduction processes of LCO no longer be provided by cobalt metal alone, and anionic oxygen is

also involved. [5,27,31] The oxidized O^{n-} species will alter the CoO_6 coordination status in cobalt oxide layers, and even be induced to release O₂. Therefore, oxygen redox reversibility is crucial to the structural reversibility and stability of the LCO cathode at high voltages. To further elucidate the boosted structural reversibility of LMP-LCO, the oxygen K-edge high-efficiency mapping of resonant inelastic X-ray scattering (mRIXS) technique with a probing depth of 100-200 nm is employed. [32,33] This technique can differentiate the intrinsic oxygen signal from the strong transitional metal character that is enlarged in the spectroscopic analysis of O K-edge, thus identifying the oxygen redox activity of LCO. Figure 4c,d show the O K-edge mRIXS mapping in bare-LCO and 2%LMP-LCO cathodes at different charge/discharge states, respectively. In pristine samples of bare-LCO and 2%LMP-LCO, the vertically extended, broad features (brown and white regions) at ≈524 eV emission energy correspond to Co–O hybridization. After charging to 4.65 V, this hybridization feature remains strong and further broadened due to the increased Co-O hybridization in highly oxidized states. More importantly, the feature of lattice oxidized oxygen merges at ≈522.3 eV emission energy (red circle). When LMP-LCO cathode is discharged to 3.0 V, the features disappear, indicating reversible oxygen redox in LMP-LCO. Strikingly, the strong signal for lattice oxidized oxygen in LMP-LCO cathode is well maintained after 50 cycles and even enhanced after 10 cycles. For a direct comparison, during the first cycle, the signal of lattice oxidized oxygen in bare-LCO appears when charged to 4.65 V and then disappears when discharged to 3.0 V, indicating oxygen redox behavior of bare-LCO similar to that of LMP-LCO cathode in the first cycle. However, after 10 cycles, the intensity of the oxidized oxygen signal decreases significantly, and after 50 cycles, the intensity is still weakened, indicating a fast decay of the oxygen redox reactions after the repeated charge/discharge process, in contrast to that of LMP-LCO. Therefore, this finding supports the idea that the LMP-LCO cathode has superior oxygen redox stability, which stabilizes the cobalt oxide layers in LCO.

To evaluate the interfacial stability of bare-LCO and LMP-LCO, post-mortem scanning electron microscopy (SEM) analyses are performed before and after cycles to monitor their surface morphologies. As shown in Figure 5a,c, after 100 charge/discharge cycles, visible micro-cracks and the exposed layer structures (red arrow) caused by the accumulation effects of stress can be observed on the surface of bare-LCO compared to its pristine sample, which suggests there is a degradation of the surface structure. The direct exposure of the interior structure to electrolytes will lead to an increase in cobalt leaching and a sharp decay in capacity after prolonged cycling at high voltages. In contrast, the surface of LMP-LCO particles remains intact (Figure 5b,d), is uniformly distributed, and has no cracks after 100 cycles. To further analyze the effect of LMP coating on interfacial stability, the *operando* differential electrochemical mass spectrometry (DEMS) experiments are performed to capture gas evolution during the first charge of bare-LCO and 2%LMP-LCO to 4.65 V, as shown in Figure 5e,f. Irrespective of the cycling profile, gas O2, which is largely related to the activity of oxygen on the cathodes' surface, is detected above 4.0 V versus Li⁺/Li for both bare-LCO and LMP-LCO; however, near 4.40-4.65 V, the O₂ gas released from the LMP-LCO cathode is much less than that of the bare-LCO. It is suggested that the LMP modification could

16136829, 2023, 39, Downloaded from https

.com/doi/10.1002/smll.202300802 by University Town Of Shenzhen, Wiley Online Library on [23/11/2025]. See the Terms

on Wiley Online Library for rules of use; OA articles are governed by the applicable Creative Commons

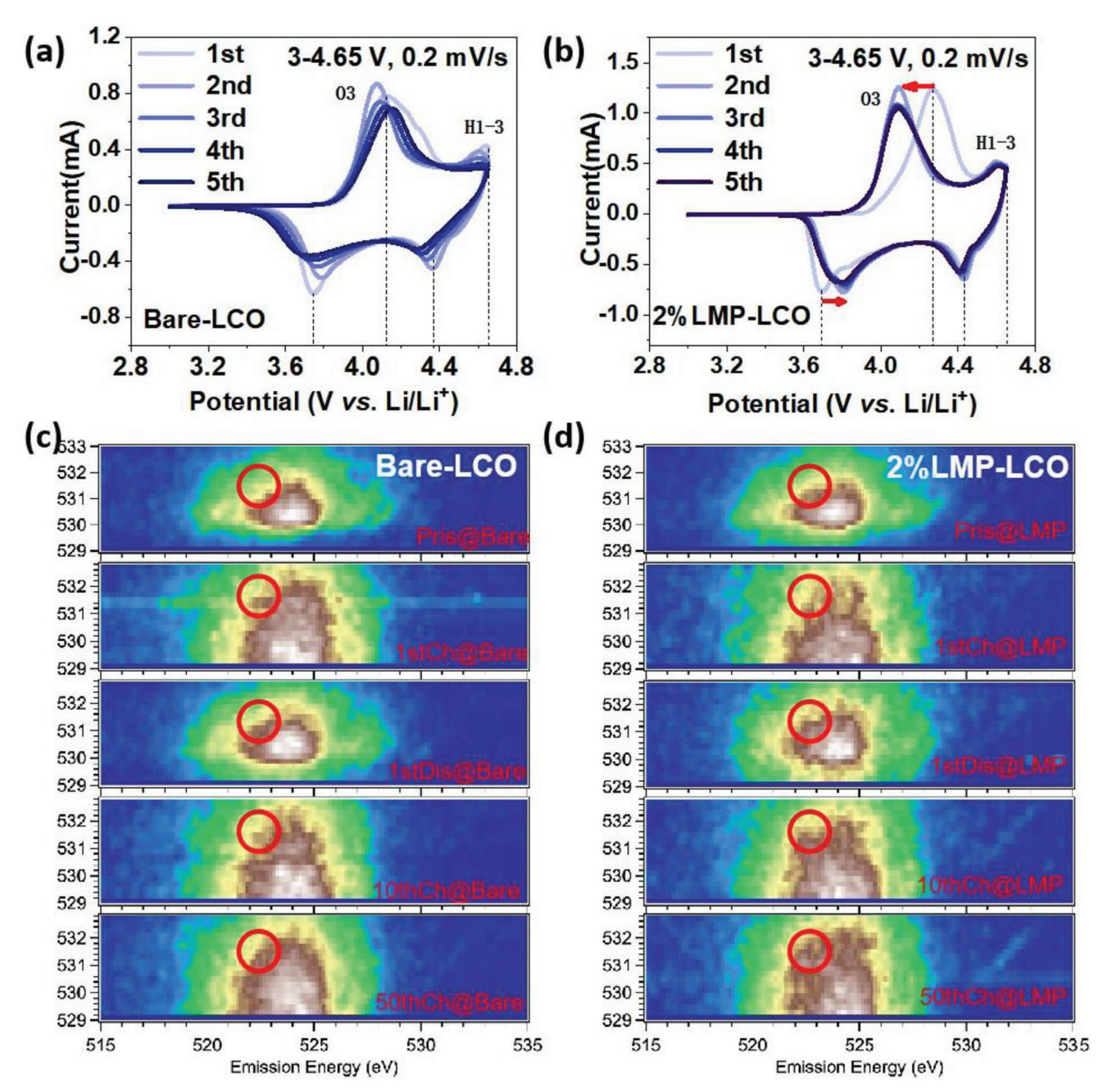


Figure 4. a,b) Cyclic voltammetry of cells with bare-LCO and 2%LMP-LCO at a scan rate of 0.2 mV s⁻¹ within 3.0–4.65 V, respectively. c,d) The O K-edge mRIXS mapping of the bare-LCO and 2%LMP-LCO cathodes at different charge/discharge states.

efficiently suppress the evolution of O_2 gas. Meanwhile, the released CO_2 gas for the LMP-LCO, which is usually derived from the carbonate-electrolyte decomposition reactions at high voltages, is also smaller than that of the bare-LCO. Therefore, the LMP modification on LCO can hinder the formation of highly reactive oxygen radical during the electrochemical process.

It is natural to ask why the LMP modification promotes structural reversibility, i.e., redox reversibility of Co and O ions in Mgdoped LCO (Mg-LCO, in **Figure 6**a). To this end, we have analyzed the geometrical and electronic structure for LCO with and without Mg-dopant by the DFT method. One thing to note is that

oxygen redox is often ascribed to the covalency of the transition metal and oxygen bonds. [11,34] Many theoretical studies and experiments have proved that oxygen would be involved in the redox reaction of cathodes due to the net charge density gains or losses around oxygen. [35,36] Therefore, the oxygen redox reversibility can be improved by properly reducing the covalent strength of the Co–O bonds. The energy difference between the transition metal (TM) and oxygen band centers, i.e., Δ , reflects the covalent and ionic strength of the TM–O bonds. The significant increase of Δ (less covalent strength) suggests that the TMs are mostly responsible for the redox process. Figure 6b shows the projected

16136829, 2023, 39, Downloaded from https://onlinelibrary.wiley.com/doi/10.1002/smll.202300802 by University Town Of Shenzhen, Wiley Online Library on [23/11.2025]. See the Terms and Conditions (https://onlinelibrary.wiley.com/terms

nditions) on Wiley Online Library for rules of use; OA articles are governed by the applicable Creative Commons License

www.small-journal.com

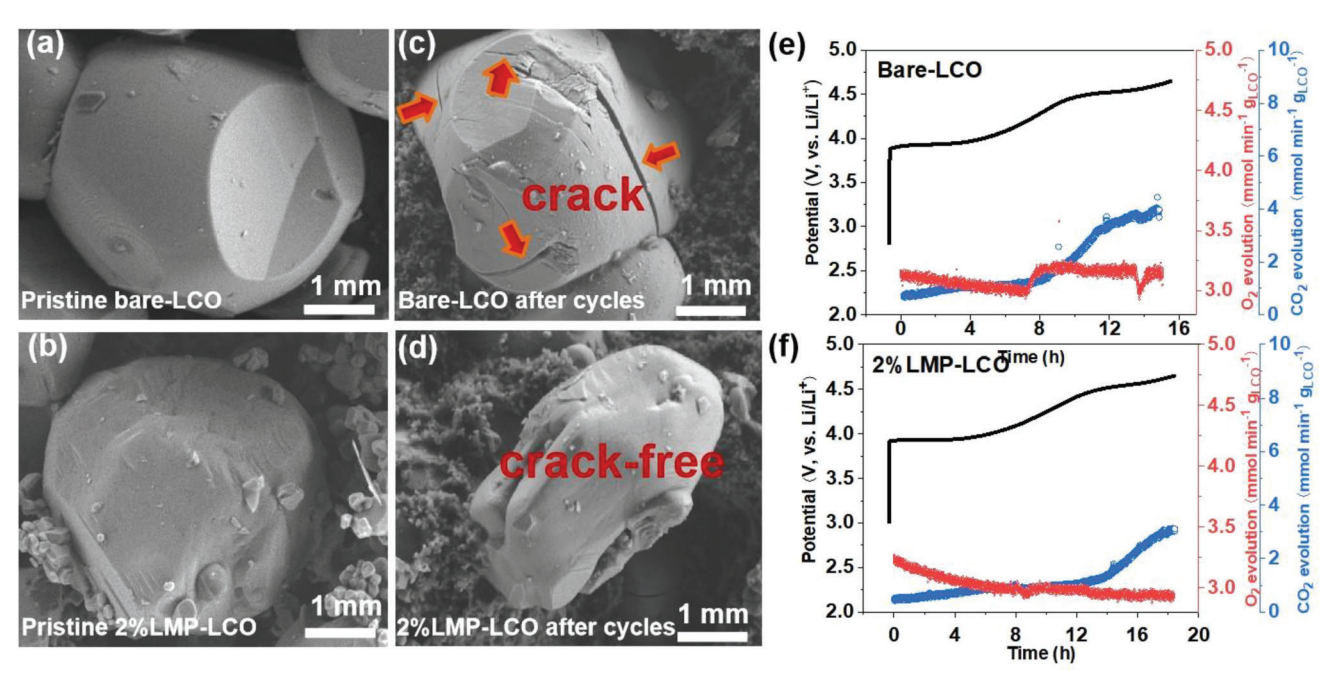


Figure 5. a–d) SEM images of bare-LCO (a,c) and 2%LMP-LCO (b,d) before and after 100 cycles. e,f) DEMS during charging the bare-LCO and 2%LMP-LCO cathode to 4.65 V, respectively.

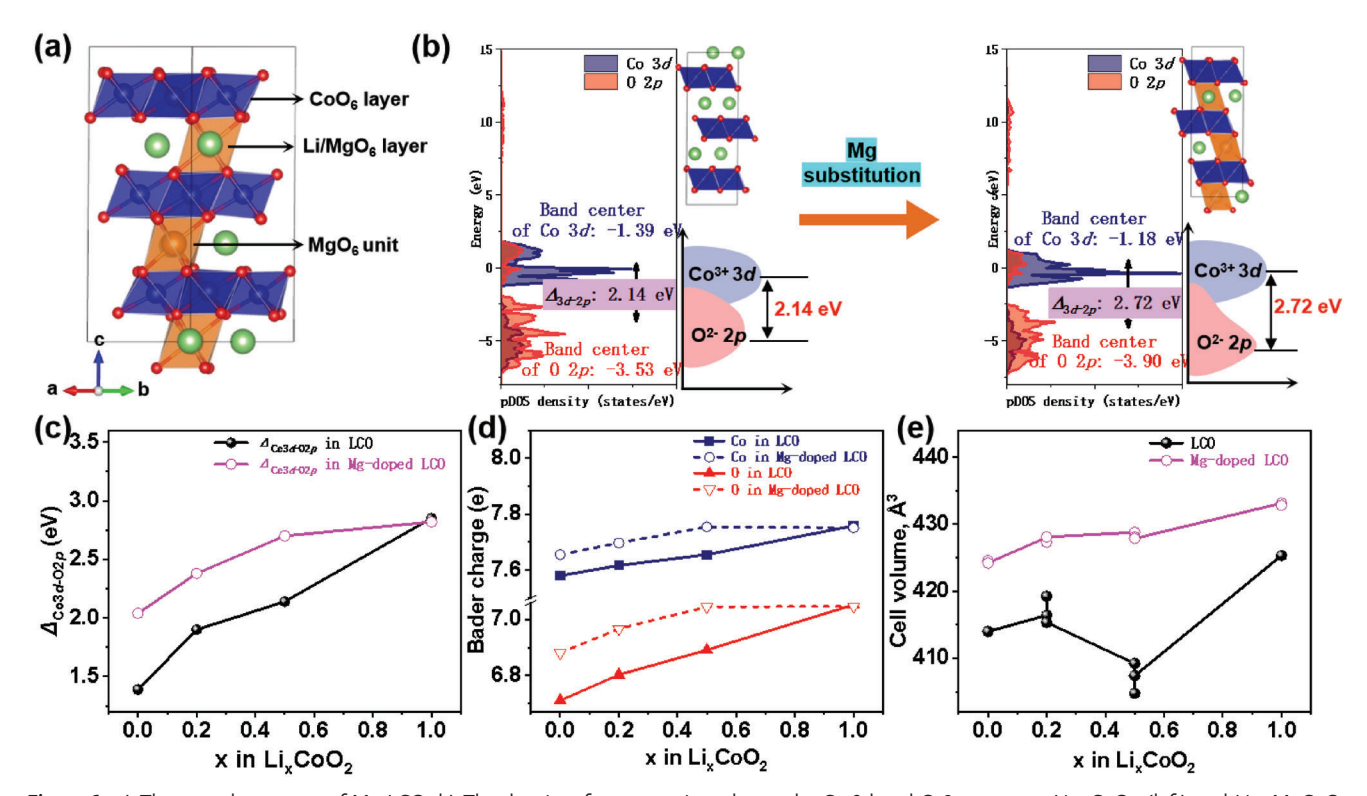


Figure 6. a) The crystal structure of Mg-LCO. b) The density of states projected over the Co 3d and O 2p states at $\text{Li}_{0.5}\text{CoO}_2$ (left) and $\text{Li}_{0.5}\text{MgCoO}_2$ (right) with the schematic orbital energy diagram of Co 3d and O 2p states to evaluate the influence on the electron structure change of Co and O by the Mg-doping. c) The $\Delta_{\text{Co3}d-\text{O2}p}$ -composition profile for LCO with and without Mg-dopant, where $\Delta_{\text{Co3}d-\text{O2}p}$ is the energy gap between Co 3d and O 2p band center. d) The Bader charge of Co and O ions with the increase of Li content in LCO and Mg-LCO. e) The cell volume-composition profile for LCO and Mg-LCO.

16136829, 2023, 3, 9. Downloaded from https://onlinelbrary.wi.ele.com/doi/10.1002/smll.202308020 by University Town Of Shenzhen, Wiley Online Library on [23/112025]. See the Terms and Conditions (https://onlinelibrary.wiley.com/terms-and-conditions) on Wiley Online Library for rules of use; OA articles are governed by the applicable Creative Commons Licensee

density of states (pDOS) of the Co 3d and O 2p orbitals in the LCO and Mg-LCO with the band structure of the redox mechanism. The energy difference calculated through the results of pDOS. Δ , expands \approx 0.58 eV after Mg-doping, from 2.14 to 2.72 eV. Electron removal from this scenario is more likely to result in an adequately positioned band for triggering reversible anionic redox. In other words, this reduces the probability of neighboring oxygen bonds (O-O) by electron transfer and enhances the stability of the oxygen skeleton. And more pDOS calculations in Li_vCoO₂ $(0 \le x \le 1)$ (Figure 6c; Figure S14, Supporting Information) further demonstrate that Mg-doped LCO always has a larger Δ than that of pure LCO. Figure 6d shows that the Bader charges of Co and O in Mg-LCO are always larger than those in pure LCO at different delithiated states, indicating Co cations have fewer positive charges and O anions have more negative charges. This result is consistent with the prediction of energy difference, i.e., Mg-doping reduces the covalency of Co-O bonds. More importantly, the Bader charge results (Figure 6d) also indicate that Mgdoping in Li-sites will lower the average valence state of Co, i.e., $+(3-\delta)$. The low valence states of Co on the surface can inhibit the highly oxidized states on the particle surface even at high voltages, which mitigates the detrimental side reactions through decoupling Co redox and O redox. The cell volume change in Figure 6e shows delithiated process causes a gradual decrease of cell volume in Mg-LCO, but jagged-like changes for pure LCO (decreases first, then increases, and last decreases). Therefore, Mg cations in the LCO act as pillars to stabilize crystal structure during the charge-discharge processes and prevent fatigue crack brought by cumulative strain and stress.[37,37] In addition, Mgdoping slightly reduces the bandgaps of LCO at delithiated states (Figure S14, Supporting Information). Therefore, the above analysis suggests the reversibility of the phase transitions during the charge-discharge cycling, which is confirmed above by mRIXS, SEM, and DEMS results.

3. Conclusion

In summary, a facile but effective approach to surface modification based on the sol-gel method has been applied to one-step create bulk Mg-doping and surface LMP-LPO coating for LCO cathode without causing structural destruction. The co-modified LCO, i.e., LMP-LCO, shows an initial discharge capacity of 203.6 mAh g⁻¹ and 71.76% capacity retention after 200 cycles between 3.0 and 4.65 V. It's worth noting that initial capacity loss for the first five cycles is quite severe but from 5th to 200th cycle, 2%LMP-LCO can achieve capacity retention of 81.8% and 81.3% at a cut-off voltage of 4.60 and 4.65 V, respectively. The capacity retention of LMP-LCO with 4.70 and 4.80 V cutoff cycling is still comparable with that with 4.65 V, indicating the excellent stability of the LMP-LCO. Excitingly, the LMP-LCO cathode exhibits a specific capacity of up to 120.8 mAh g⁻¹ at the high current density of 5 C at the cut-off voltage of 4.65 V. Experimental characterizations and DFT calculations have been employed to prove that the optimization of both the bulk and surface leads to high structural reversibility and interfacial stability. Moreover, the Mg-pillars not only improve lattice oxygen redox by decreasing the O 2p band center and tailoring the energy gap between the O 2p and Co 3d band centers but also further decrease the lattice strain and stress to prevent cracks and breakages.

Consequently, the structural stability of the LMP-LCO cathode material is enhanced, which improves capacity retention after long-term cycling. The Mg-doping changes the intrinsic electronic structure of LCO cathode materials, thus affecting their redox reactions during charge-discharge processes, especially oxygen redox. This work provides a new avenue for the study of highvoltage LCO batteries and a reference for the large-scale processing of commercial LCO cathode materials. It is also hopeful to develop a series of LMP@layered Ni-Co-Mn or Ni-Co-Al, etc. to maintain excellent stability of the layered structure under high voltages.

4. Experimental Section

Preparation of LMP-LCO: Bare-LCO was provided by Xiamen Tungsten Co., Ltd (XTC). Ltd. LMP-LCO with different weight percentages of LMP (1%, 2%, and 3%) were synthesized via a sol-gel and calcination process. Typically, the amount of CH₃COOLi·2H₂O, C₄H₆MgO₄·4H₂O, and NH4H2PO4 was calculated (in the case of forming 2% LMP-LCO, $CH_3COOLi \cdot 2H_2O : C_4H_6MgO_4 \cdot 4H_2O : NH_4H_2PO_4 = 0.051 g : 0.102 g$: 0.055 g), First, CH₃COOLi·2H₂O and C₄H₆MgO₄·4H₂O were sequentially added to beaker A containing CH₃CH₂O (20 g) and C₆H₈O₇·H₂O (2 g), stirred at room temperature until completely dissolved, and C-LCO (3 g) was added to beaker A and stirred at 80 °C for 10 min. NH₄H₂PO₄ was added to beaker B containing 5 mL of deionized water and stirred at 80 °C until completely dissolved. The solution in beaker B was added dropwise to beaker A, and kept stirring at 80 °C until the liquid appeared to gel. The mixture in beaker A was then dried in a vacuum drying oven (100 °C, 12 h). The dried mixture was thoroughly ground into powder and was calcinated at 800 °C for 2 h with a heating and cooling rate of 5 °C min^{-1} to get LMP-LCO.

Cells Assembling: The positive electrode was by mixing 80 wt.% cathode, 10% conductive agent (Super P), 10% binder (PVDF), and Nmethylpyrrolidone (NMP) evenly to get slurry, the slurry is uniformly poured on the aluminum collector, and then vacuum drying at 120 °C for 12 h, then cut into a diameter of 14 mm disk system. In a glove box filled with argon gas ($H_2O/O_2 < 0.01$ ppm), the LCO/Li and LMP-LCO/Li coin half-cells (CR2016) were assembled using the prepared positive electrode and lithium foil as a negative electrode and polypropylene diaphragm. The liquid electrolytes were composed of 1 M LiPF₆ and ethylene carbonate/ethyl methyl carbonate (EMC) (EC/EMC = 3:7, V/V).

Electrochemical Tests: The galvanostatic discharge/charge measurements of with LCO cathodes were conducted within 3-4.60 V, 3-4.65 V, 3-4.70 V, and 3-4.80 V using the battery testing system (LAND, Wuhan) under room temperature (25 °C). The cyclic voltammetry of LCO/Li and LMP-LCO/Li half cells was tested by CHI760E electrochemical workstation with a scanning range of 3.0-4.65 V and a scanning speed of 0.2 mV s⁻¹. The Electrochemical alternating current impedance (EIS) was measured using the CHI760E electrochemical workstation in the frequency range of 10^6-10^{-1} Hz and under 5 mV disturbance. The GITT curves of the cell were performed with a 20 min discharge at 53 µA followed by a 40 min relaxation.

Materials Characterization: The XRD data were collected on a Rigaku MiniFlex600 powder diffractometer using a Cu K α source ($\lambda = 1.5418$ Å) in the range of $2\theta = 10.0-90.0^{\circ}$, with a step length of 0.02° , and each step was 2s. The surface morphology and element distribution of the materials before and after reduction were analyzed by a field emission scanning electron microscope (FESEM, JEOL JSM6700) and EDS. The coating layer on the surface of LCO was analyzed by a high-resolution transmission electron microscopy (HRTEM, JEOL JEM-2100F) at an accelerating voltage of pprox200 kV. The 2%LMP-LCO samples were prepared by a focused ion beam (FIB). An X-ray photoelectron spectroscopy (Thermo ESCALAB 250Xi) was used to surface of samples by-product generation, and the binding energies reported herein were corrected regarding C 1s peak of the C-C/C-H at 284.4 eV. An Al K α monochromatized radiation (h = 1486.6 eV) was

employed as an X-ray source. The surface of the specimen was sputtered by inert gas ion bombardment with a sputter rate of 15 nm (SiO $_2$ as standard reference) for each time, and spectra were then collected from the center of an etched area. Survey spectra were recorded with a pass energy of 0.125 eV, and high-resolution spectra were recorded with a pass energy of 0.02 eV. O-K mRIXS of LCO electrodes before and after cycles was determined by the X-ray absorption spectra (XAS) at the American Light source (ALS). The obtained data were analyzed by Athena software. The excitation energy resolution was $\approx\!0.35$ eV, and the emission energy resolution was $\approx\!0.25$ eV. The excitation energy step of all mappings was 0.2 eV. mRIXS were collected at each excitation energy. Finally, the final 2D image was obtained by normalization, integration, and combination of the beam flux and acquisition time.

Calculation Methods: All DFT calculations were performed using first-principles density functional theory-based calculations as implemented in the Vienna ab initio simulation package (VASP) within the projector augmented-wave approach. [38,39] The exchange-correlation functional utilized was at the generalized gradient approximation level proposed by Perdew–Burke–Ernzerhof (GGA-PBE). [40,41] Cut-off energy of 500 eV was used for all calculations. The k-point sampling grids are set to $4\times4\times3$ for the LiCoO2 system with 48 atoms. The Mg-doped LCO system was built on the 48-atom LiCoO2 system by replacing one Mg²⁺ with two Li⁺-ions. All atomic coordinates along with the lattice constants of the LCO and Mg-doped LCO were optimized fully until the force convergence criterion of 0.01 eV Å⁻¹ was reached.

Supporting Information

Supporting Information is available from the Wiley Online Library or from the author.

Acknowledgements

J.Z. and W.Z. contributed equally to this work. This research work was supported by Province Natural Science fund of Guangdong (2022A1515012476). [Correction added after publication 27 September 2023: All corresponding authors were correctly identified.]

Conflict of Interest

The authors declare no conflict of interest.

Data Availability Statement

Research data are not shared.

Keywords

bulk Mg-doping, high-voltage LiCoO $_2$, lithium-ion batteries, surface LiMgPO $_4$ /Li $_3$ PO $_4$ coating

Received: February 28, 2023 Revised: May 9, 2023 Published online: May 31, 2023

- [1] Z. Lin, T. Liu, X. Ai, C. Liang, Nat. Commun. 2018, 9, 5262.
- [2] F. Wu, J. Maier, Y. Yu, Chem. Soc. Rev. 2020, 49, 1569.
- [3] Y. Lyu, X. Wu, K. Wang, Z. Feng, T. Cheng, Y. Liu, M. Wang, R. Chen, L. Xu, J. Zhou, Y. Lu, B. Guo, Adv. Energy Mater. 2021, 11, 2000982.

- [4] L. Wang, B. Chen, J. Ma, G. Cui, L. Chen, Chem. Soc. Rev. 2018, 47, 6505.
- [5] J. Qian, L. Liu, J. Yang, S. Li, X. Wang, H. L. Zhuang, Y. Lu, *Nat. Commun.* 2018, 9, 4918.
- [6] W. Xue, R. Gao, Z. Shi, X. Xiao, W. Zhang, Y. Zhang, Y. G. Zhu, I. Waluyo, Y. Li, M. R. Hill, Z. Zhu, S. Li, O. Kuznetsov, Y. Zhang, W.-K. Lee, A. Hunt, A. Harutyunyan, Y. Shao-Horn, J. A. Johnson, J Li, Energy Environ. Sci. 2021, 14, 6030.
- [7] C. Sun, X. Liao, F. Xia, Y. Zhao, L. Zhang, S. Mu, S. Shi, Y. Li, H. Peng, G. Van Tendeloo, K. Zhao, J Wu, ACS Nano 2020, 14, 6181.
- [8] J. Li, C. Lin, M. Weng, Y. Qiu, P. Chen, K. Yang, W. Huang, Y. Hong, J. Li, M. Zhang, C. Dong, W. Zhao, Z. Xu, X. Wang, K. Xu, J. Sun, F. Pan, Nat. Nanotechnol. 2021, 16, 599.
- [9] M. D. Radin, S. Hy, M. Sina, C. Fang, H. Liu, J. Vinckeviciute, M. Zhang, M. S. Whittingham, Y. S. Meng, A. Van der Ven, Adv. Energy Mater. 2017, 7, 1602888.
- [10] Y. Jiang, C. Qin, P. Yan, M. Sui, J. Mater. Chem. A 2019, 7, 20824.
- [11] A. Fu, Z. Zhang, J. Lin, Y. Zou, C. Qin, C. Xu, P. Yan, K. Zhou, J. Hao, X. Yang, Y. Cheng, D.-Y. Wu, Y. Yang, M.-S. Wang, J. Zheng, Energy Storage Mater. 2022, 46, 406.
- [12] X. Ding, D. Luo, J. Cui, H. Xie, Q. Ren, Z. Lin, Angew. Chem., Int. Ed. 2020, 59, 7778.
- [13] L. Feng, Z. Yin, C. Wang, Z. Li, S. Zhang, P. Zhang, Y. Deng, F. Pan, B. Zhang, Z Lin, Adv. Funct. Mater. 2023, 33, 2210744.
- [14] C.-W. Wang, Y. Zhou, J.-H. You, J.-D. Chen, Z. Zhang, S.-J. Zhang, C.-G. Shi, W.-D. Zhang, M.-H. Zou, Y. Yu, J.-T. Li, L.-Y. Zeng, L. Huang, S.-G. Sun, ACS Appl. Energy Mater. 2020, 3, 2593.
- [15] X. Wang, Q. Wu, S. Li, Z. Tong, D. Wang, H. L. Zhuang, X. Wang, Y. Lu, Energy Storage Mater. 2021, 37, 67.
- [16] C.-W. Wang, Nano Energy 2023, 108, 108192.
- [17] X. Yang, C. Wang, P. Yan, T. Jiao, J. Hao, Y. Jiang, F. Ren, W. Zhang, J. Zheng, Y. Cheng, X. Wang, W. Yang, J. Zhu, S. Pan, M. Lin, L. Zeng, Z. Gong, J. Li, Y. Yang, Adv. Energy Mater. 2022, 12, 2200197.
- [18] S. Kalluri, M. Yoon, M. Jo, S. Park, S. Myeong, J. Kim, S. X. Dou, Z. Guo, J Cho, Adv. Energy Mater. 2017, 7, 1601507.
- [19] J.-N. Zhang, Q. Li, C. Ouyang, X. Yu, M. Ge, X. Huang, E. Hu, C. Ma, S. Li, R. Xiao, W. Yang, Y. Chu, Y. Liu, H. Yu, X.-Q. Yang, X. Huang, L. Chen, H Li, Nat. Energy 2019, 4, 594.
- [20] G. Amatucci, J. M. Tarascon, L. C. Klein, Solid State Ionics 1996, 83,
- [21] R. V. Chebiam, A. M. Kannan, F. Prado, A. Manthiram, Electrochem. Commun. 2001, 3, 624.
- [22] K. S. Ganesh, B. Wang, J.-S. Kim, B. Zhu, J. Phys. Chem. C 2019, 123,
- [23] X. Ren, X. Zhang, Z. Shadike, L. Zou, H. Jia, X. Cao, M. H. Engelhard, B. E. Matthews, C. Wang, B. W. Arey, X. Yang, J. Liu, J. Zhang, W. Xu, Adv. Mater. 2020, 32, 2004898.
- [24] L. Dahéron, R. Dedryvère, H. Martinez, M. Ménétrier, C. Denage, C. Delmas, D. Gonbeau, Chem. Mater. 2008, 20, 583.
- [25] X. Yang, M. Lin, G. Zheng, J. Wu, X. Wang, F. Ren, W. Zhang, Y. Liao, W. Zhao, Z. Zhang, N. Xu, W. Yang, Y. Yang, Adv. Funct. Mater. 2020, 30, 2004664.
- [26] M. Wang, X. Feng, H. Xiang, Y. Feng, C. Qin, P. Yan, Y. Yu, Small Methods 2019, 3, 1900355.
- [27] W. M. Seong, K. Yoon, M. H. Lee, S.-K. Jung, K. Kang, *Nano Lett.* 2019, 19, 29.
- [28] D. Takamatsu, Y. Koyama, Y. Orikasa, S. Mori, T. Nakatsutsumi, T. Hirano, H. Tanida, H. Arai, Y. Uchimoto, Z Ogumi, Angew. Chem., Int. Ed. 2012, 51, 11597.
- [29] W. Yang, Nat. Energy 2018, 3, 619.
- [30] X. Yang, C. Wang, P. Yan, T. Jiao, J. Hao, Y. Jiang, F. Ren, W. Zhang, J. Zheng, Y. Cheng, X. Wang, W. Yang, J. Zhu, S. Pan, M. Lin, L. Zeng, Z. Gong, J. Li, Y. Yang, Adv. Energy Mater. 2022, 12, 2200197.
- [31] W. Kong, J. Zhang, D. Wong, W. Yang, J. Yang, C. Schulz, X. Liu, Angew. Chem., Int. Ed. 2021, 60, 27102.

www.advancedsciencenews.com



16136829, 2023, 39, Downloaded from https://onlinelibrary.wiley.com/doi/10.1002/smll.202300802 by University Town Of Shenzhen, Wiley Online Library on [23/11/2025]. See the Terms

conditions) on Wiley Online Library for rules of use; OA articles are governed by the applicable Creative Commons License

www.small-journal.com

- [32] X. Liu, G.-L. Xu, V. S. C. Kolluru, C. Zhao, Q. Li, X. Zhou, Y. Liu, L. Yin, Z. Zhuo, A. Daali, J.-J. Fan, W. Liu, Y. Ren, W. Xu, J. Deng, I. Hwang, D. Ren, X. Feng, C. Sun, L. Huang, T. Zhou, M. Du, Z. Chen, S.-G. Sun, M. K. Y. Chan, W. Yang, M. Ouyang, K. Amine, Nat. Energy 2022, 7, 808
- [33] W. Yang, T. P. Devereaux, J. Power Sources 2018, 389, 188.
- [34] W. Huang, Q. Zhao, M. Zhang, S. Xu, H. Xue, C. Zhu, J. Fang, W. Zhao, G. Ren, R. Qin, Q. Zhao, H. Chen, F. Pan, Adv. Energy Mater. 2022, 12, 2200813.
- [35] G. Assat, J.-M. Tarascon, Nat. Energy 2018, 3, 373.

- [36] M. Zhang, D. A. Kitchaev, Z. Lebens-Higgins, J. Vinckeviciute, M. Zuba, P. J. Reeves, C. P. Grey, M. S. Whittingham, L. F. J. Piper, A. Van der Ven, Y. S. Meng, Nat. Rev. Mater. 2022, 7, 522.
- [37] Y. Huang, Y. Zhu, H. Fu, M. Ou, C. Hu, S. Yu, Z. Hu, C. Chen, G. Jiang, H. Gu, H. Lin, W. Luo, Y. Huang, Angew. Chem. 2021, 133, 4732.
- [38] G. Kresse, J. Furthmüller, Phys. Rev. B 1996, 54, 11169.
- [39] G. Kresse, D. Joubert, Phys. Rev. B 1999, 59, 1758.
- [40] J. P. Perdew, K. Burke, M. Ernzerhof, *Phys. Rev. Lett.* **1996**, *77*, 3865.
- [41] P. E. Blöchl, *Phys. Rev. B* **1994**, *50*, 17953.